Coexistence of superconductivity and antiferromagnetism in the Hubbard model for cuprates

A. Foley,[1] S. Verret,[1] A.-M. S. Tremblay,[1,2] and D. Sénéchal[1]
[1]*Département de physique and Institut quantique, Université de Sherbrooke, Sherbrooke, Québec, Canada J1K 2R1*
[2]*Canadian Institute for Advanced Research, Toronto, Ontario, Canada M5G 1Z8*

(Received 28 November 2018; revised manuscript received 25 March 2019; published 21 May 2019)

Antiferromagnetism and d-wave superconductivity are the most important competing ground-state phases of cuprate superconductors. Using cellular dynamical mean-field theory for the Hubbard model, we revisit the question of the coexistence and competition of these phases in the one-band Hubbard model with realistic band parameters and interaction strengths. With an exact diagonalization solver, we improve on previous works with a more complete bath parametrization which is carefully chosen to grant the maximal possible freedom to the hybridization function for a given number of bath orbitals. Compared with previous incomplete parametrizations, this general bath parametrization shows that the range of microscopic coexistence of superconductivity and antiferromagnetism is reduced for band parameters for $Nd_{2-x}Ce_xCuO_4$ (NCCO) and confined to electron doping with parameters relevant for $YBa_2Cu_3O_{7-x}$ (YBCO).

DOI: 10.1103/PhysRevB.99.184510

I. INTRODUCTION

The proximity of antiferromagnetism (AF) with superconductivity (SC) is common in unconventional superconductors: Bechgaard salts, heavy-fermion superconductors, high-temperature superconductors (cuprates), iron pnictides, and selenides can all go from antiferromagnetic to superconducting upon varying some parameter (doping, pressure, etc.). Microscopic, i.e., spatially homogeneous, coexistence of superconductivity with antiferromagnetism is a definite possibility in iron pnictides [1] and selenides [2], in the heavy-fermion compound $CeRhIn_5$ [3,4], and in electron-doped cuprate superconductors [5]. In this respect, hole-doped cuprates are quite different: the only magnetic phase with which superconductivity coexists is an incommensurate spin-density wave [6–9]. A clear difficulty is to distinguish microscopic coexistence (a pure phase) from macroscopic coexistence resulting from inhomogeneities in the sample or from thermodynamic separation of competing phases.

The antiferromagnetic phase breaks rotation symmetry $[SO(3)]$ and can be characterized by an order parameter $\mathbf{M}$, the staggered magnetization. Superconductivity, on the other hand, breaks the $U(1)$ symmetry associated with electron number conservation, and the associated order parameter is the pairing amplitude Δ. A signature of the microscopic coexistence of these two phases would be the presence of the so-called π-triplet order parameter [10–12], which is necessarily nonzero if both $\mathbf{M}$ and the d-wave order parameter Δ are nonzero. Note that the π triplet is a kind of pair-density wave [13–15]. However, it is different from the pair-density wave observed experimentally in scanning tunneling microscopy [16]. A unified description of the two broken symmetries can be formulated in the language of $SO(5)$ symmetry [10]. A phenomenological Landau-Ginzburg theory of the interplay and coexistence of the two phases can also be formulated without reference to the $SO(5)$ description [11].

The issue of a possible AF-SC coexistence in high-T_c superconductors has been addressed theoretically using the one-band Hubbard model and its strong-coupling limit, the t-J model. Inui *et al.* found microscopic AF-SC coexistence in a slave-boson (mean-field) treatment of the Hubbard model [17]. Himeda and Ogata found it in a variational Monte Carlo study of the t-J model [12]. The presence of the π-triplet order parameter was studied in the mean-field approximation by Kyung [18], also in the t-J model. Beyond the mean-field approximation, microscopic AF-SC coexistence was predicted to occur within the Hubbard model with the variational cluster approximation (VCA) [19] and cluster dynamical mean-field theory (CDMFT) [20,21]. In Ref. [20], microscopic coexistence for the nearest-neighbor hopping model was found only for small interaction strength ($U \leqslant 8t$). Functional renormalization group (FRG) methods, although more relevant to weak and moderate coupling, also predict the occurrence of such a microscopic coexistence phase [22,23].

The lack of microscopic coexistence of superconductivity with commensurate antiferromagnetism in hole-doped cuprates casts some doubt on the prediction of quantum cluster methods or on the relevance of the one-band Hubbard model to these materials. In this paper, we show that a more careful application of CDMFT to the one-band Hubbard model makes this AF-SC microscopic coexistence disappear in models relevant to hole-doped cuprates while reducing its range in a model of electron-doped cuprates. We use a CDMFT impurity solver based on exact diagonalization at zero temperature, like in Refs. [20,21], and compare the simple parametrization that they used with the most general parametrization of the bath orbitals, as used in Refs. [24–26]. Quantum Monte Carlo (QMC) solvers, especially state-of-the-art continuous-time solvers [27], are free of bath parametrization ambiguities. Up to now, the superconducting [28–42] and AF phases [28,43,44] have only been studied separately using continuous time solvers. In principle, the question of

coexistence can be addressed with these approaches, but this has yet to be done.

A QMC cluster-size scaling study [45] demonstrated that 2×2 plaquettes give reasonably well converged results, and exponential convergence of local observables with cluster size was observed [46–48]. Because of this and since a 2×2 cluster is already very close to the limit of what is feasible with exact diagonalization (ED) CDMFT given the computational resources available to us, we consider only that one size of cluster.[1]

This paper is organized as follows: In Sec. II we present the model and explain the method used (ED-CDMFT), with particular attention to the bath parametrization. In Sec. III we present and discuss our results, before concluding.

II. MODEL AND METHOD

Although high-temperature superconductors are charge-transfer insulators [49], they are often modeled by the one-band Hubbard model on a square lattice:

$$H = -\sum_{\mathbf{r},\mathbf{r}',\sigma} t_{\mathbf{r},\mathbf{r}'} c^\dagger_{\mathbf{r},\sigma} c_{\mathbf{r}',\sigma} + U \sum_{\mathbf{r}} n_{\mathbf{r}\uparrow} n_{\mathbf{r}\downarrow} - \mu \sum_{\mathbf{r},\sigma} n_{\mathbf{r}\sigma}. \quad (1)$$

The hopping amplitudes $t_{\mathbf{r},\mathbf{r}'}$ depend on the particular compound and are restricted to nearest neighbor (t), second neighbor (t'), and third neighbor (t''). We use two sets of parameters: one for $YBa_2Cu_3O_{7-x}$ (YBCO) ($t'/t = -0.3$, $t''/t = 0.2$) [50], a hole-doped compound, and one for $Nd_{2-x}Ce_xCuO_4$ (NCCO) ($t'/t = -0.17$, $t''/t = 0.03$) [51], an electron-doped compound. The first-neighbor hopping t defines the energy scale and is set to unity ($t = 1$). The NCCO hoppings can also be considered representative of a class of hole-doped cuprates to which $La_{2-x}Sr_xCuO_4$ (LSCO) belongs (see Fig. 5 of Ref. [52]).

A. Cluster dynamical mean-field theory

In CDMFT, for the purpose of computing the electron self-energy $\mathbf{\Sigma}$, the above model is replaced by a cluster model (in this paper, a four-site plaquette) immersed in an effective medium. With an exact diagonalization solver, this medium is represented by a finite set of uncorrelated bath orbitals hybridized with the cluster sites. This discretization of the medium is an additional approximation that must be made to accommodate an ED solver and as such can lead to additional finite-size effects [24]. These bath orbitals, together with the cluster, are described by an Anderson impurity model (AIM):

$$H_{\text{imp}} = H_{\text{clus}} + \sum_{\alpha,\xi} (\theta_{\alpha\mu} c^\dagger_\alpha a_\mu + \text{H.c.}) + \sum_{\mu,\nu} \epsilon_{\mu\nu} a^\dagger_\mu a_\nu, \quad (2)$$

where H_{clus} is the restriction of the Hubbard Hamiltonian (1) to the cluster. a_ν annihilates an electron on the bath orbital labeled ν (ν stands for both orbital and spin indices, and so does α for cluster orbitals). The matrix $\theta_{\alpha\mu}$ defines the hybridization between the bath and cluster, and $\epsilon_{\mu\nu}$ defines the dynamics of the bath. The bath parameters $\theta_{\alpha\mu}$ and $\epsilon_{\mu\nu}$ are determined by an iterative procedure, as explained below.

The one-electron Green's function $\mathbf{G}'$ takes the following form as a function of complex frequency ω:

$$\mathbf{G}'^{-1}(\omega) = \omega - \mathbf{t} - \mathbf{\Gamma}(\omega) - \mathbf{\Sigma}(\omega), \quad (3)$$

where the hybridization matrix $\mathbf{\Gamma}(\omega)$ is defined as

$$\mathbf{\Gamma}(\omega) = \boldsymbol{\theta}(\omega - \boldsymbol{\epsilon})^{-1}\boldsymbol{\theta}^\dagger \quad (4)$$

in terms of the matrices $\theta_{\alpha\mu}$ and $\epsilon_{\alpha\beta}$. In practice, the cluster Green's function is computed from an exact diagonalization technique, and the self-energy is extracted from Eq. (3).

The Green's function $\mathbf{G}(\tilde{\mathbf{k}}, \omega)$ for the original lattice Hubbard model is then computed from the cluster's self-energy as

$$\mathbf{G}^{-1}(\tilde{\mathbf{k}}, \omega) = \mathbf{G}_0^{-1}(\tilde{\mathbf{k}}, \omega) - \mathbf{\Sigma}(\omega). \quad (5)$$

Here $\tilde{\mathbf{k}}$ denotes the wave vectors belonging to the Brillouin zone associated with the superlattice of plaquettes, and $\mathbf{G}_0$ is the noninteracting lattice Green's function. All Green's-function-related quantities are $2N_c \times 2N_c$ matrices, with $N_c = 4$ being the number of sites in the plaquette.

The bath parameters are ideally determined by the self-consistency condition $\mathbf{G}'(\omega) = \bar{\mathbf{G}}(\omega)$, where

$$\bar{\mathbf{G}}(\omega) \equiv \int \frac{d^2\tilde{k}}{(2\pi)^2} \mathbf{G}(\tilde{\mathbf{k}}, \omega) \quad (6)$$

and the integral is carried over the reduced Brillouin zone (the domain of $\tilde{\mathbf{k}}$). In other words, the local Green's function $\mathbf{G}'(\omega)$ should coincide with the Fourier transform $\bar{\mathbf{G}}(\omega)$ of the full Green's function at the origin of the superlattice. This condition should hold at all frequencies, which is impossible in ED-CDMFT because of the finite number of bath parameters $\boldsymbol{\epsilon}$ and $\boldsymbol{\theta}$ at our disposal. Thus, the self-consistency condition is replaced by a minimization of the so-called *distance function*:

$$d = \sum_{\omega_n} W(i\omega_n) \,\text{Tr}\, |\mathbf{G}'^{-1}(i\omega_n) - \bar{\mathbf{G}}^{-1}(i\omega_n)|^2, \quad (7)$$

with respect to the bath parameters for a given value of $\mathbf{\Sigma}$. The weight function $W(x)$ is meant to give more importance to small frequencies, and a fictitious temperature is used to define the grid of Matsubara frequencies over which the above merit function is evaluated. Details can be found, for instance, in Refs. [21,53–55]. In this work, we use a fictitious temperature $\beta = 50/t$ and set $W(i\omega_n)$ to 1 if $\omega_n < \omega_c$, with $\omega_c = 2t$; $W(i\omega_n)$ is set to zero for higher Matsubara frequencies.

To summarize, the ED-CDMFT procedure runs as follows:

(1) An initial, trial set of bath parameters is chosen.

(2) The ED solver is applied to Hamiltonian (2) and provides a numerical representation of $\mathbf{G}'$ that allows for a quick computation of $\mathbf{G}'(\omega)$, and hence of $\mathbf{\Sigma}(\omega)$, at any complex frequency.

(3) The Fourier transform $\bar{\mathbf{G}}(\omega)$ is computed for the set of Matsubara frequencies appearing in (7).

(4) A new set of bath parameters $\{\theta_{\alpha\mu}, \varepsilon_{\mu\nu}\}$ is obtained by minimizing the distance function (7).

[1] With the bath structure being simpler in one dimension, computations with more than four correlated orbitals are possible with an ED solver [24].

(5) We go back to step 2 with the new set of bath parameters until convergence is achieved.

Note that superconductivity is allowed in the procedure through the use of the Nambu formalism, by which a particle-hole transformation is performed on the spin-down orbitals (e.g., $c_{\alpha,\downarrow} \to c^\dagger_{\alpha,\downarrow}$). This does not require a doubling of the degrees of freedom in the Green's function if no spin-flip terms are present in the model, which is the case here. With eight bath orbitals, we introduce two Nambu spinors, one for the cluster and one for the bath:

$$C = (c_{1\uparrow} \cdots c_{4\uparrow}, c^\dagger_{1\downarrow} \cdots c^\dagger_{4\downarrow}), \tag{8}$$

$$A = (a_{1\uparrow} \cdots a_{8\uparrow}, a^\dagger_{1\downarrow} \cdots a^\dagger_{8\downarrow}). \tag{9}$$

The noninteracting part of Hamiltonian (2) then takes the general form

$$H_{\mathrm{imp},0} = (C^\dagger, A^\dagger)\begin{pmatrix} \mathbf{T} & \boldsymbol{\theta} \\ \boldsymbol{\theta}^\dagger & \boldsymbol{\epsilon} \end{pmatrix}\begin{pmatrix} C \\ A \end{pmatrix}, \tag{10}$$

where the matrices $\boldsymbol{\theta}$ and $\boldsymbol{\epsilon}$ can now contain anomalous terms.

Two different bath parametrizations are used in this paper, as described in the next section. They parametrize the same number of bath orbitals, but they differ in the number of free parameters that are set by the CDMFT procedure. The first bath parametrization is essentially the same as the one used in Ref. [21]; the second, inspired by Refs. [24,25], contains many more independent parameters. One may naturally expect that increasing the number of bath parameters brings the system closer to perfect self-consistency. Using the second parametrization gives us the best possible self-consistency for a given number of orbitals; this is where this paper improves upon previous studies. On the other hand, the CDMFT procedure itself becomes more time-consuming, particularly optimizing the merit function (7).

B. Simple bath parametrization

A simple and intuitive way to configure the bath orbitals for a four-site plaquette is illustrated in Fig. 1. Time and memory constraints limit the number of bath orbitals to 8, for a total of 12 orbitals in the AIM [Eq. (2)]. The eight bath orbitals are separated into two sets, numbered 1 and 2, each with four orbitals. Each set can be thought of as a "ghost" of the plaquette, with a site energy ε_i $(i = 1, 2)$, hybridized with the bath through a hopping amplitude θ_i. The presence of superconductivity in the effective medium is characterized by a singlet pairing amplitude Δ_i with opposite signs along the x and y directions, in accordance with d-wave symmetry. This makes a total of six independent parameters, as summarized in Fig. 1(a). If only superconductivity is probed, the AIM has a C_{2v} symmetry (horizontal and vertical reflexions), and only those six bath parameters are used.

If antiferromagnetism is considered as well, then the symmetry is reduced to C_2 (a π rotation). Six additional parameters are introduced, as illustrated in Fig. 1(b): spin antisymmetric bath energies ε^{AF}_i and hybridizations θ^{AF}_i that alternate in sign between sites and triplet-pairing amplitudes π_i whose signs are defined in the figure (via arrows). This makes a total of 12 independent bath parameters.

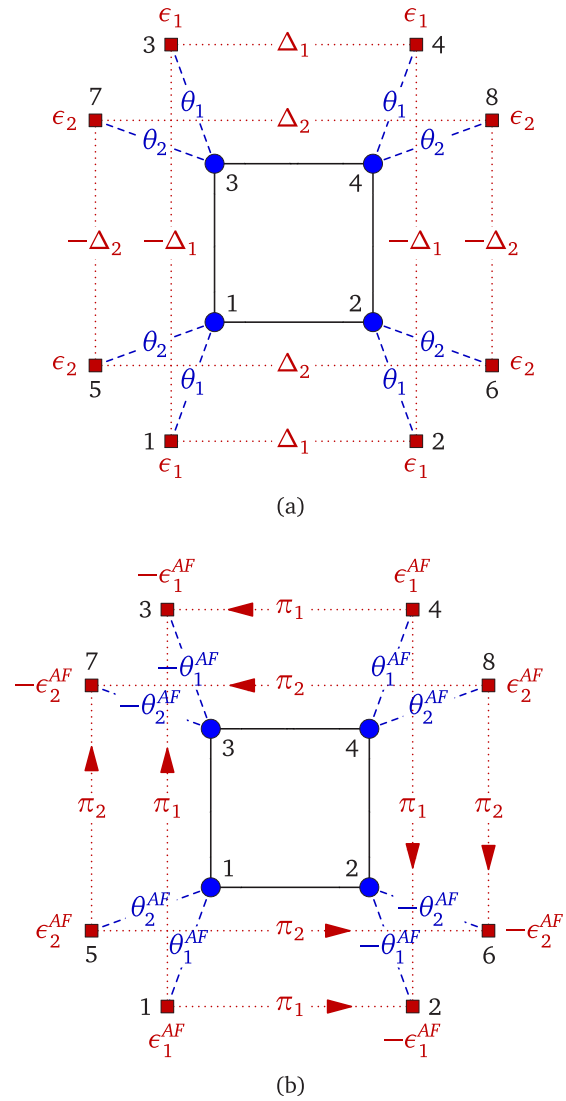

FIG. 1. Schematic description of the simple bath parametrization. The blue circles represent the cluster sites, and red squares show the bath orbitals. Intrabath terms are shown in red, and hybridization terms are shown in blue. Cluster and bath orbitals are numbered separately. (a) Terms used when not probing antiferromagnetism, with C_{2v} symmetry. (b) Additional terms needed when probing antiferromagnetism and breaking C_{2v} down to C_2. See text for details.

Let us specify the matrices introduced in Eq. (10). We order the bath orbitals so the two sets of four spin-up orbitals are consecutive and followed by the two sets of spin-down orbitals, in the same order. Overall, the 16×16 matrix $\boldsymbol{\epsilon}$ associated with this bath model has the following structure in terms of 4×4 blocks:

$$\boldsymbol{\epsilon} = \begin{pmatrix} E_1 + E_1^{AF} & 0 & D_1 & 0 \\ 0 & E_2 + E_2^{AF} & 0 & D_2 \\ D_1 & 0 & -E_1 + E_1^{AF} & 0 \\ 0 & D_2 & 0 & -E_2 + E_1^{AF} \end{pmatrix}, \tag{11}$$

where $E_i = \varepsilon_i \mathbf{1}_{4\times4}$, $E_i^{AF} = \varepsilon_i^{AF}\,\mathrm{diag}(1,-1,-1,1)$, and

$$D_i = \begin{pmatrix} 0 & -\Delta_i+\pi_i & \Delta_i-\pi_i & 0 \\ -\Delta_i-\pi_i & 0 & 0 & \Delta_i+\pi_i \\ \Delta_i+\pi_i & 0 & 0 & -\Delta_i-\pi_i \\ 0 & \Delta_i-\pi_i & -\Delta_i+\pi_i & 0 \end{pmatrix}. \tag{12}$$

The minus signs in the bottom half of the $\boldsymbol{\epsilon}$ matrix come from the Nambu representation of spin-down orbitals. On the other hand, the 8×16 matrix $\boldsymbol{\theta}$ has the following structure:

$$\boldsymbol{\theta} = \begin{pmatrix} \Theta_1+\Theta_1^{AF} & \Theta_2+\Theta_2^{AF} & 0 & 0 \\ 0 & 0 & -\Theta_1+\Theta_1^{AF} & -\Theta_2+\Theta_2^{AF} \end{pmatrix}, \tag{13}$$

where $\Theta_i = \theta_i \mathbf{1}_{4\times4}$, $\Theta_i^{AF} = \theta_i^{AF}\,\mathrm{diag}(1,-1,-1,1)$.

C. General bath parametrization

The bath parametrization defined above is not the most general one. In order to construct the most general bath appropriate to each point group (C_{2v} and C_2), one must first realize that any unitary transformation of the bath orbitals is possible and that this gauge freedom must be fixed somehow. We do this by requiring (1) that the matrix $\boldsymbol{\epsilon}$ be diagonal and (2) that it falls into irreducible representations of the symmetry group of the AIM.

If only superconductivity is probed, we can impose C_{2v} symmetry (horizontal and vertical reflexions) on the AIM. In addition to C_{2v} symmetry, we also assume spin symmetry, which reduces the number of independent parameters. C_{2v} has four distinct irreducible representations, each of which we associate with two bath orbitals for a total of eight, the same number as in the simple parametrization in the previous section. We label these orbitals from 1 to 8, in two consecutive series of four, each series corresponding to the four irreducible representations: 1 and 5 in the first representation, 2 and 6 in the second, 3 and 7 in the third, and 4 and 8 in the fourth. Figure 2(a) illustrates the hybridization of the first four orbitals. The coefficients θ_i and Δ_i are the parameters present in the hybridization between the cluster and the ith bath orbital: θ_i is the amplitude of the simple hoppings, and Δ_i is the amplitude of the singlet pairing operators.

In this bath parametrization, the matrix $\boldsymbol{\epsilon}$ is diagonal: $\mathrm{diag}(\varepsilon_i)\oplus\mathrm{diag}(-\varepsilon_i)$, with $i=1,\ldots,8$. Again, the last eight components correspond to the spin-down orbitals in the Nambu representation (hence the minus sign).

The hybridization matrix $\boldsymbol{\theta}$, on the other hand, is a dense 8×16 matrix:

$$\boldsymbol{\theta} = \begin{pmatrix} \Theta & -D \\ D & -\Theta \end{pmatrix}, \tag{14}$$

where the 4×8 blocks Θ and D are defined as

$$\Theta = \begin{pmatrix} \theta_1 & \theta_2 & \theta_3 & \theta_4 & \theta_5 & \theta_6 & \theta_7 & \theta_8 \\ \theta_1 & \theta_2 & -\theta_3 & -\theta_4 & \theta_5 & \theta_6 & -\theta_7 & -\theta_8 \\ \theta_1 & -\theta_2 & \theta_3 & -\theta_4 & \theta_5 & -\theta_6 & \theta_7 & -\theta_8 \\ \theta_1 & -\theta_2 & -\theta_3 & \theta_4 & \theta_5 & -\theta_6 & -\theta_7 & \theta_8 \end{pmatrix}, \tag{15}$$

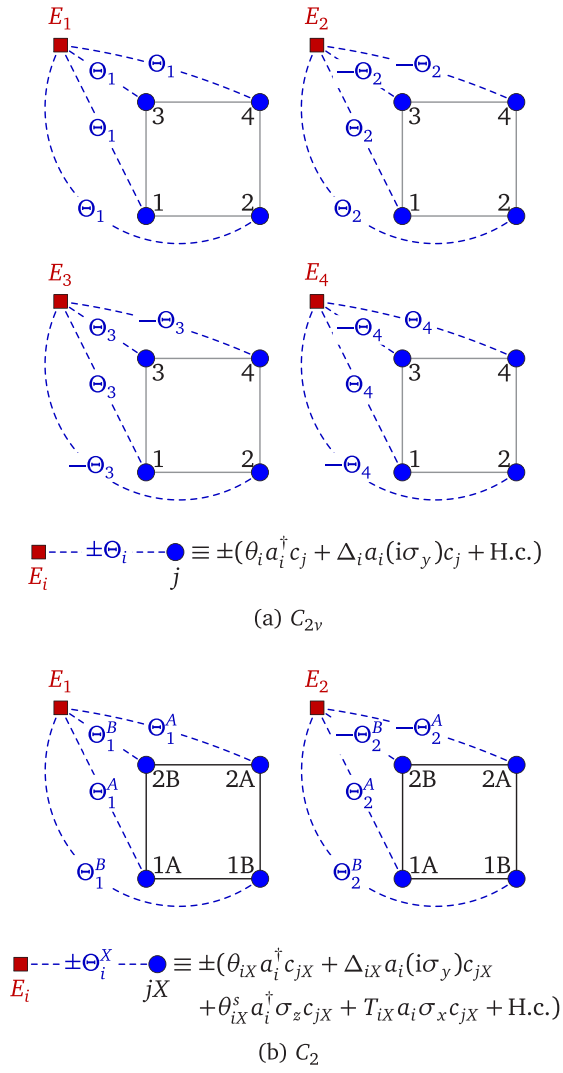

FIG. 2. (a) Schematic description of the general parametrization of the bath when probing superconductivity with C_{2v} symmetry. Blue circles represent the cluster sites, and red squares show the bath orbitals. The four panels correspond to the first four bath orbitals, each associated with a different irreducible representation of C_{2v}. The blue dashed lines and accompanying symbols represent a hybridization operator as defined below the panels. The four diagrams correspond to the first four columns (or the last four columns) of expressions (15) and (16) in the text. (b) The same as in (a) for C_2 symmetry, used when probing antiferromagnetism and superconductivity. The operators symbolized by the dashed line are once again defined below the panels. The superscripts A and B correspond to the two sublattices when AF order is present. In the equations in (a) and (b), spinor notation is used: The Pauli matrices define the spin part of each term.

$$D = \begin{pmatrix} \Delta_1 & \Delta_2 & \Delta_3 & \Delta_4 & \Delta_5 & \Delta_6 & \Delta_7 & \Delta_8 \\ \Delta_1 & \Delta_2 & -\Delta_3 & -\Delta_4 & \Delta_5 & \Delta_6 & -\Delta_7 & -\Delta_8 \\ \Delta_1 & -\Delta_2 & \Delta_3 & -\Delta_4 & \Delta_5 & -\Delta_6 & \Delta_7 & -\Delta_8 \\ \Delta_1 & -\Delta_2 & -\Delta_3 & \Delta_4 & \Delta_5 & -\Delta_6 & -\Delta_7 & \Delta_8 \end{pmatrix}. \tag{16}$$

The number of independent bath parameters is 8 in $\boldsymbol{\epsilon}$ and $2\times8=16$ in $\boldsymbol{\theta}$, for a total of 24.

If antiferromagnetism is probed as well, the symmetry reduces to C_2, which has only two irreducible representations.

Since we can afford eight bath orbitals, we associate four bath orbitals with each irreducible representation, with the same pattern as the C_{2v} bath. Namely, all the odd-labeled bath orbitals have the same structure as the first orbital, and all the even bath orbitals have the same structure as the second orbital. The cluster-bath couplings of the first and second bath orbitals are illustrated in Fig. 2(b). The superscripts A and B refer to the two sublattices induced by antiferromagnetic order. The parameters associated with different sublattices may differ.

The energy E_i ($i = 1, \ldots, 8$) has a component ε_i even in spin and a component ε_i^s odd in spin, which makes $2 \times 8 = 16$ parameters. Thus, the diagonal matrix $\boldsymbol{\epsilon}$ has the structure

$$\left(\varepsilon_1 + \varepsilon_1^s, \ldots, \varepsilon_8 + \varepsilon_8^s, -\varepsilon_1 + \varepsilon_1^s, \ldots, -\varepsilon_8 + \varepsilon_8^s\right). \tag{17}$$

The operators Θ_i^A in Fig. 2(b) contain four parameters each: θ_i^A, θ_i^{sA}, Δ_i^A, and T_i^A, where θ_i^A is a spin-symmetric hopping operator, θ_i^{sA} is a spin-antisymmetric hopping, Δ_i^A is a singlet pairing, and T_i^A is a triplet pairing, with similar notation for Θ_i^B. This makes eight parameters for each bath index i and therefore $8 \times 8 = 64$ hybridization parameters in total. The hybridization matrix $\boldsymbol{\theta}$ has the following form:

$$\boldsymbol{\theta} = \begin{pmatrix} \Theta + \Theta^s & -D + T \\ D + T & -\Theta + \Theta^s \end{pmatrix}, \tag{18}$$

where the 4×8 block Θ is defined as

$$\Theta = \begin{pmatrix} \theta_1^A & \theta_2^A & \theta_3^A & \theta_4^A & \theta_5^A & \theta_6^A & \theta_7^A & \theta_8^A \\ \theta_1^B & \theta_2^B & \theta_3^B & \theta_4^B & \theta_5^B & \theta_6^B & \theta_7^B & \theta_8^B \\ \theta_1^B & -\theta_2^B & \theta_3^B & -\theta_4^B & \theta_5^B & -\theta_6^B & \theta_7^B & -\theta_8^B \\ \theta_1^A & -\theta_2^A & \theta_3^A & -\theta_4^A & \theta_5^A & -\theta_6^A & \theta_7^A & -\theta_8^A \end{pmatrix},$$

with similar notation for Θ^s (with components θ_i^{sA}, θ_i^{sB}), D (with components Δ_i^A, Δ_i^B), and T(with components T_i^A, T_i^B). The total number of independent bath parameters in this parametrization is $16 + 64 = 80$. Note that any hybridization function that can be produced with the simple parametrization can also be produced by the general parametrization we described. By applying a unitary transformation to the simple parametrization, we could obtain a bath Hamiltonian with the same structure as the general parametrization, except for a large number of additional constraints between bath parameters.

D. Order parameters

Once a CDMFT solution is found, various order parameters may be computed. The quantities of interest are the averages of the following operators defined on the lattice:

$$\hat{M} = \sum_{\mathbf{r}} e^{i\mathbf{Q}\cdot\mathbf{r}}[c_{\mathbf{r}\uparrow}^\dagger c_{\mathbf{r}\uparrow} - c_{\mathbf{r}\downarrow}^\dagger c_{\mathbf{r}\downarrow}], \quad \mathbf{Q} = (\pi, \pi), \tag{19}$$

$$\hat{D} = \sum_{\mathbf{r}} [c_{\mathbf{r}\uparrow} c_{\mathbf{r}+\mathbf{x}\downarrow} - c_{\mathbf{r}\downarrow} c_{\mathbf{r}+\mathbf{x}\uparrow} - c_{\mathbf{r}\uparrow} c_{\mathbf{r}+\mathbf{y}\downarrow} + c_{\mathbf{r}\downarrow} c_{\mathbf{r}+\mathbf{y}\uparrow}] + \text{H.c.}, \tag{20}$$

$$\hat{\pi} = \sum_{\mathbf{r}} e^{i\mathbf{Q}\cdot\mathbf{r}}[c_{\mathbf{r}\uparrow} c_{\mathbf{r}+\mathbf{x}\downarrow} + c_{\mathbf{r}\downarrow} c_{\mathbf{r}+\mathbf{x}\uparrow} - c_{\mathbf{r}\uparrow} c_{\mathbf{r}+\mathbf{y}\downarrow} - c_{\mathbf{r}\downarrow} c_{\mathbf{r}+\mathbf{y}\uparrow}] + \text{H.c.} \tag{21}$$

The first is just the spin-density operator with the antiferromagnetic wave vector $\mathbf{Q}$. The second defines the d-wave pairing operator: singlet pairing on nearest-neighbor bonds $\mathbf{x}$ and $\mathbf{y}$ with opposite signs. The third is the π-triplet operator: triplet pairing on nearest-neighbor bonds with opposite signs along $\mathbf{x}$ and $\mathbf{y}$ and a spatial modulation defined by the antiferromagnetic wave vector $\mathbf{Q}$.

In ED-CDMFT, there are two ways to estimate the average of one-body operators. The first, and also the simplest, consists of computing the expectation value of the restriction of these operators to the cluster in the ground state of the impurity model. The averages obtained in this way will be called *cluster averages*.

The second method involves the lattice model Green's function (5). Specifically, the average of any one-body operator of the form $\hat{O} = O_{\alpha\beta} c_\alpha^\dagger c_\beta$ can be computed from the Green's function as

$$\langle \hat{O} \rangle = \oint \frac{d\omega}{2\pi} \operatorname{tr}[\mathbf{O}\mathbf{G}(\omega)]. \tag{22}$$

The frequency integral is taken along a contour that surrounds the negative real axis. In practice, this is done in the mixed basis of superlattice wave vectors $\tilde{\mathbf{k}}$ and cluster orbital indices, knowing that both $\mathbf{O}$ and $\mathbf{G}$ are diagonal in $\tilde{\mathbf{k}}$:

$$\langle \hat{O} \rangle = \oint \frac{d\omega}{2\pi} \int \frac{d^2\tilde{k}}{(2\pi)^2} \operatorname{tr}[\mathbf{O}(\tilde{\mathbf{k}})\mathbf{G}(\tilde{\mathbf{k}}, \omega)]. \tag{23}$$

The averages obtained in this way will be called *lattice averages*.

An operator $\hat{O}$ that is defined on only sites, not on bonds, like $\hat{M}$ above or the electron density $\hat{n}$, will be called a *local operator*. For such an operator $\mathbf{O}(\tilde{\mathbf{k}})$ does not depend on $\tilde{\mathbf{k}}$, and the above formula simplifies to

$$\langle \hat{O} \rangle = \oint \frac{d\omega}{2\pi} \operatorname{tr}[\mathbf{O}\bar{\mathbf{G}}(\omega)], \tag{24}$$

where the local Green's function $\bar{\mathbf{G}}$ is defined in Eq. (6). For a local operator, the cluster average, instead of being computed from the impurity ground state, could alternatively be computed from Eq. (24), but with the impurity Green's function $\mathbf{G}'$ substituted for $\bar{\mathbf{G}}$, which yields the cluster average mentioned before.

Cluster and lattice averages are not equal for two reasons. First, operators that live on bonds, like $\hat{D}$ and $\hat{\pi}$, differ from their restrictions to the cluster: Intercluster bonds are ignored. Lattice averages take these intercluster bonds into account; cluster averages do not. Second, in ED-CDMFT the self-consistency is only approximate; therefore, the local Green's function $\bar{\mathbf{G}}$ is not exactly the same as the impurity Green's function $\mathbf{G}'$. Thus, even for a local operator, for which Eq. (24) applies, the lattice average will be only approximately the same as the cluster average.

III. RESULTS

In this section we present zero-temperature phase diagrams: the order parameters as a function of density for two sets of band parameters and five values of U. We display cluster averages for local operators (electron density $\hat{n}$ and staggered magnetization $\hat{M}$) and lattice averages for bond operators ($\hat{D}$ and $\hat{\pi}$). See the Supplemental Material for other combinations and for comments on the differences between

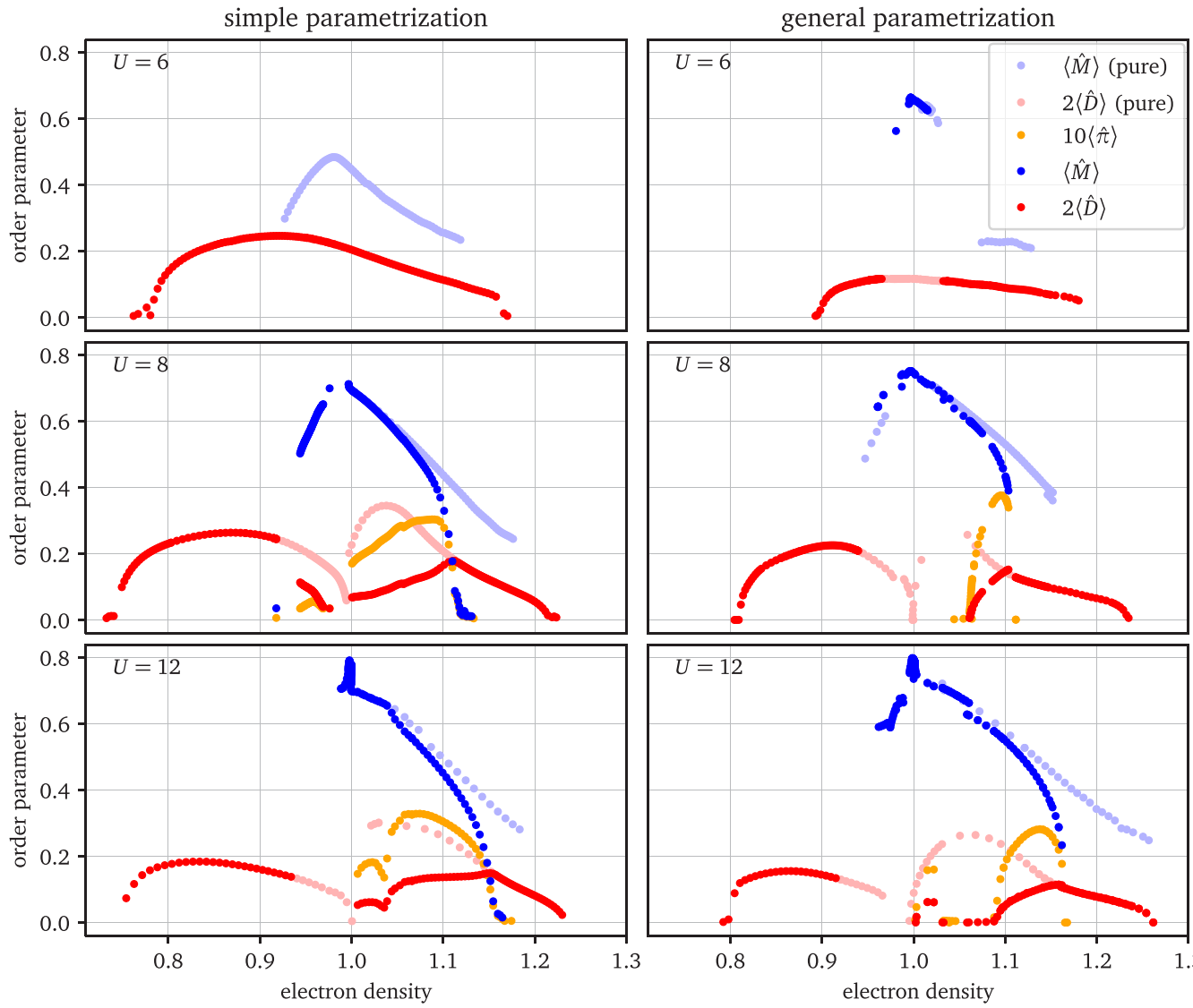

FIG. 3. Phase diagrams (order parameter as a function of electron density) obtained with the simple (left) and general (right) bath parametrizations, with YBCO-like band parameters ($t'/t = -0.3$, $t''/t = 0.2$) and three values of on-site repulsion U. Blue symbols represent the AF order parameter $\langle\hat{M}\rangle$, red symbols show the dSC order parameter $\langle\hat{D}\rangle$ (times 2), and the orange symbols give the π-triplet order (times 10). Dark symbols are obtained when allowing microscopic coexistence of the two orders. Light symbols are obtained when probing pure solutions. Deep in the superconducting regime, the dark symbols can be from pure SC simulations; allowing for AFM there would have significantly increased computational time with no benefits.

them [56]. The lowest value of U for each set (YBCO- and NCCO-like) lies below the Mott transition; hence, superconductivity, when probed alone, extends all the way to half filling. The other values of U are above the Mott transition, and hence, superconductivity vanishes exactly at half filling in the underdoped regime. In larger clusters, both in Dynamical cluster approximation (DCA) with a quantum Monte Carlo solver [33] and in exact diagonalization with the variational cluster approximation [57], it is found that d-wave superconductivity starts away from half filling.

A. YBCO-like parameters

Figure 3 shows the AF and d-wave superconductivity (dSC) order parameters obtained in CDMFT for a one-band dispersion appropriate for YBCO and three values of U (6, 8, and 12) as a function of electron density n (half filling corresponds to $n = 1$). The left panels show the solutions obtained using the simple parametrization of Sec. II B, and the right panels show the solutions obtained using the general parametrization of Sec. II C. Even though YBCO is a hole-doped compound, we have obtained solutions on both the hole- and electron-doped sides of the phase diagram.

Solutions were obtained either by allowing both orders to emerge simultaneously in microscopic coexistence or by allowing only one order at a time, suppressing the other. For instance, in the simple parametrization, antiferromagnetism is suppressed by forcing the bath parameters illustrated in the Fig. 1(b) to zero. Similarly, suppressing superconductivity is done by setting to zero all bath pairing operators ($\Delta_{1,2}$

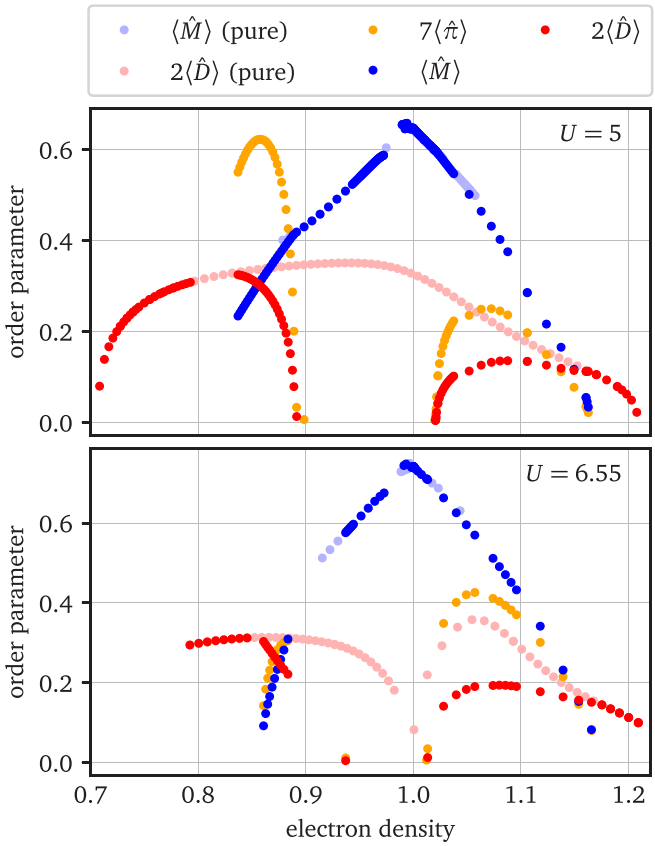

FIG. 4. Phase diagrams (order parameter as a function of electron density) obtained with the general bath representations, with NCCO-like band parameters ($t'/t = -0.17$, $t''/t = 0.03$) and two values of on-site repulsion U. Symbols have the same meaning as in Fig. 3. Note that the dSC order parameter is multiplied by 2, and the π-triplet order parameter is multiplied by 7 for clarity.

and $\pi_{1,2}$). Even when both orders are allowed, microscopic coexistence does not necessarily happen: one of the two orders (AF or dSC) may dominate, in which case the variational parameters of the other order (dSC or AF) reach zero by the end of the self-consistency loop. To construct our phase diagrams, we let the self-consistency procedure choose which phase is the right one, rather than comparing ground-state energy. We proceed this way because thermodynamic potentials are unreliable with a small finite bath.

In Figs. 3 and 4, dark symbols indicate the order parameter (blue for AF and red for dSC) in the microscopically coexistent or dominant solution. Light symbols indicate subdominant solutions, i.e., solutions obtained by suppressing one order in the coexisting regime. Orange circles denote the average of the π-triplet operator of Eq. (21), which is nonzero in regions of microscopic AF-dSC coexistence.

One notices the following features:

(1) Microscopic coexistence does not occur at $U = 6$ in both simple and general bath parametrizations. It occurs only at $U = 8$ and, in a wider range of doping, at $U = 12$.

(2) In the general parametrization, microscopic coexistence occurs only on the electron-doped side, whereas it also occurs on the hole-doped (i.e., physical) side in the simple parametrization.

(3) The pure antiferromagnetic solutions show many discontinuities, especially on the hole-doped side and at stronger coupling and in the more general parametrization.

(4) Where microscopic coexistence occurs with the general parametrization, the transitions from a pure phase to microscopic coexistence are of second order.

(5) A small superconducting region can be seen around $n = 1.01$ at $U = 12$ with the general parametrization. This is a finite-size effect due to a change in the number of particles in the AIM. On either side of this small dome, the AIM has a well-defined number of particles. The small superconducting order parameter breaks particle number conservation and allows the change in the number of particles to happen smoothly over a finite range of doping, instead of abruptly as it would if particle number conservation were enforced.

(6) On the hole-doped side, the transition from superconductivity to antiferromagnetism is of first order, and the two solutions are separated in density. In principle, this leads to a macroscopic phase coexistence.

B. NCCO-like parameters

Figure 4 shows the same quantities for band parameters adequate for NCCO and two values of U. One can make the following observations:

(1) Microscopic coexistence occurs on both sides of the phase diagram for both values of U considered.

(2) On the hole-doped side, the transition from microscopic coexistence to pure SC (upon decreasing n) is discontinuous for $U = 5$; the two solutions (pure SC and microscopic coexistence) are separated in density, which leads, in principle, to macroscopic phase coexistence. Macroscopic coexistence between a pure SC phase and a microscopic SC-AF coexistence phase was seen before in VCA for different band parameters [58].

(3) On the hole-doped side, the transition from microscopic coexistence to pure AF (upon increasing n) is discontinuous at $U = 6.55$ and continuous at $U = 5$.

(4) On the electron-doped (i.e. physical) side, the transition to microscopic coexistence is continuous for both values of U.

IV. DISCUSSION

On general grounds, the phase diagrams in Fig. 3 obtained with the general parametrization should be more representative of the result obtained with an infinite bath, in other words, closer to an accurate solution of the Hubbard model. Since we find that the results for this general parametrization are closer to the experimental phase diagram of cuprates, the appropriateness of the one-band Hubbard model for cuprate superconductors is reinforced.

On physical grounds, we can argue that the phase diagrams obtained with the general parametrization are more accurate. Consider U slightly below the critical value for the Mott transition, in our case at $U = 6$: The simple parametrization leads to a superconducting ground state at half filling, whereas the general parametrization favors antiferromagnetism. The latter result is more sensible considering antiferromagnetism at half filling can be obtained at the Hartree-Fock level, while d-wave superconductivity is a dynamical effect. Another example is

the reentrant behavior of superconductivity upon underdoping obtained with the simple parametrization at $U = 12$, between half filling and 4% electron doping: It is inexplicable on physical grounds. This reentrant behavior is suppressed when using the general parametrization: there is a slight reduction in amplitude, and it appears at lower electron doping, before 3%. It also becomes well separated from the superconducting dome. This distance from the dome allows for a meaningful analysis of the particle number of the AIM on each side of this reentrant feature and leads us to believe that it is a finite-size effect, as pointed out in Sec. III A.

One can observe in Fig. 3 that, as U increases, the difference between the phase diagrams of the two parametrizations becomes subtler, especially on the hole-doped side. At $U = 12$, the results are qualitatively equivalent on the hole-doped side. We can only speculate on why this happens. As the general parametrization can reproduce any hybridization function the simple one can generate, it is possible the converged hybridization functions produced by the two parametrizations are more similar at higher U values. This would mean that the additional constraints of the simple parametrization become less of an issue as the states become more localized. In other words, it could mean that some of the constraints of the simple parametrization are physically meaningful at strong coupling.

Let us note that even our "simple parametrization" has more variational parameters than what was used in previous ED-CDMFT studies [20,21]. In these previous studies, the π triplet had no associated variational parameter in the AIM Hamiltonian, even if its expectation value does not vanish in the microscopic coexistence phase. These additional degrees of freedom allow for slightly stronger d-wave superconductivity, although the overall qualitative shape of the phase diagram is unchanged. One should also note that Ref. [20] considers a particle-hole-symmetric lattice, leading to notably different phase diagrams.

At intermediate coupling, the regime relevant for cuprates, details of the band structure, the value of t' in particular, are just as important as the interaction strength to determine the phase diagram, as noted in Ref. [21]. Indeed, Fig. 3, with band parameters relevant to YBCO, shows that electron-hole symmetry is strongly violated. In the general parametrization, microscopic coexistence between d-wave superconductivity and antiferromagnetism is confined to the electron-doped region. On the hole-doped side, the transition between antiferromagnetism and d-wave superconductivity is of first order for $U = 8$ and $U = 12$ for both parametrizations. Note that the wider range of doping for antiferromagnetism on the electron-doped side simply reflects the better nesting at the antiferromagnetic wave vector [19].

It is quite remarkable that the electron-doped side realizes a proposal by Sachdev [59] that the presence of d-wave superconductivity leads to a large displacement of the doping at which antiferromagnetism ends. This can be seen by comparing the end of the light blue dots for $U = 8$ or 12 with the end of the dark blue dots in Fig. 3. However, Sachdev's conjecture concerned the hole-doped compound where we do not observe this effect.

A continuous time (CT)-QMC computation [44] of the antiferromagnetic phase with $t' = -0.1$ shows that it extends to 15% hole doping, like what we can see in Fig. 4. This suggests that, with these band parameters and coupling, the presence of superconductivity has very little effect on the antiferromagnetic phase. An FRG study of microscopic coexistence [22] at weaker coupling but with similar band parameters finds a hole-doped phase diagram strikingly similar to Fig. 4 at $U = 5$. This shows that those results are robust when long wavelengths and incommensurate orders are suppressed.

Our small clusters cannot sustain waves with periods longer than two unit cells, like the charge order seen in experiments [60] or the incommensurate spin waves seen in both experiments [6–9,61] and infinite lattice weak-coupling calculations [23,62–64]. We expect that if we could probe such orders, parts of our phase diagram would be different. Indeed, a VCA study [65] has found a charge density wave with a four-unit-cell period coexisting microscopically with superconductivity on the hole-doped side. Although magnetism disappears at small doping on the hole-doped side even when superconductivity is absent, we cannot exclude that spiral order could persist to large hole dopings. This is one of the explanations offered [62] for the abrupt change in the Hall effect when one enters the pseudogap regime at low temperature and in magnetic fields sufficiently strong to destroy superconductivity. Collinear incommensurate magnetism, however, cannot explain these Hall data [66]. It has been proposed that Seebeck measurements can tell apart the various phenomenological theories for these Hall data [67].

Comparing the two sets of band parameters, we observe that increasing second- and third-neighbor hopping reduces the regions of microscopic coexistence. This is understandable from the bare band structure that shows reduced nesting in that case [52], weakening antiferromagnetism. This effect is especially pronounced on the hole-doped side. The effect of U on the amplitude of the triplet order hints that microscopic coexistence is stabler the closer the system is to the Mott transition, as the triplet order is stronger there. Increasing U also increases the domain of filling that supports microscopic coexistence on the electron-doped side. The phase transitions are generally second order, except on the hole-doped side where the transition between antiferromagnetism and superconductivity is often first order. This reflects the weakness of antiferromagnetism away from half filling on the hole-doped side.

V. CONCLUSION

Following the lead of Refs. [24–26], we used symmetry and gauge-invariance considerations to propose the most general parametrization of the bath for an exact diagonalization CDMFT solution of the Hubbard model with a four-site cluster hybridized with eight bath orbitals. The parametrization must be chosen according to the phases that are put in competition, here antiferromagnetism and d-wave superconductivity. A simpler parametrization gives qualitatively correct results only when antiferromagnetism and d-wave superconductivity do not coexist. We found phase diagrams that are much closer to observations than previous results found with simpler parametrizations.

In particular, microscopic coexistence between antiferromagnetism and d-wave superconductivity is more robust for electron-doped compounds. For large U and $|t'|$, the filling

where antiferromagnetism ends in the absence of superconductivity is much larger than in the presence of superconductivity.

Given the generality of the bath parametrization, our results are the most accurate that can be obtained with a finite bath and an exact diagonalization solver. They will be a useful guide for calculations that include an infinite bath but are performed with more resource-hungry continuous-time quantum Monte Carlo solvers.

ACKNOWLEDGMENTS

This work was supported by the Natural Sciences and Engineering Research Council of Canada (NSERC) under Grants No. RGPIN-2014-04584 and No. RGPIN-2015-05598, by the Canada First Research Excellence Fund, by the Research Chair in the Theory of Quantum Materials, and by Fond de recherche du Québec - Nature et technologies (FRQNT) (Québec). Computing resources were provided by Compute Canada and Calcul Québec.

[1] D. K. Pratt, W. Tian, A. Kreyssig, J. L. Zarestky, S. Nandi, N. Ni, S. L. Bud'ko, P. C. Canfield, A. I. Goldman, and R. J. McQueeney, Coexistence of Competing Antiferromagnetic and Superconducting Phases in the Underdoped $Ba(Fe_{0.953}Co_{0.047})_2As_2$ Compound Using X-ray and Neutron Scattering Techniques, Phys. Rev. Lett. **103**, 087001 (2009).

[2] R. H. Liu, X. G. Luo, M. Zhang, A. F. Wang, J. J. Ying, X. F. Wang, Y. J. Yan, Z. J. Xiang, P. Cheng, G. J. Ye, Z. Y. Li, and X. H. Chen, Coexistence of superconductivity and antiferromagnetism in single crystals $A_{0.8}Fe_{2\text{-}y}Se_2$ (A = K, Rb, Cs, Tl/K and Tl/Rb): Evidence from magnetization and resistivity, Europhys. Lett. **94**, 27008 (2011).

[3] G. Knebel, D. Aoki, D. Braithwaite, B. Salce, and J. Flouquet, Coexistence of antiferromagnetism and superconductivity in $CeRhIn_5$ under high pressure and magnetic field, Phys. Rev. B **74**, 020501(R) (2006).

[4] S. Kawasaki, T. Mito, Y. Kawasaki, G.-q. Zheng, Y. Kitaoka, D. Aoki, Y. Haga, and Y. Ōnuki, Gapless Magnetic and Quasiparticle Excitations due to the Coexistence of Antiferromagnetism and Superconductivity in $CeRhIn_5$: A Study of ^{115}In NQR under Pressure, Phys. Rev. Lett. **91**, 137001 (2003).

[5] N. P. Armitage, P. Fournier, and R. L. Greene, Progress and perspectives on electron-doped cuprates, Rev. Mod. Phys. **82**, 2421 (2010).

[6] K. Yamada, C. H. Lee, K. Kurahashi, J. Wada, S. Wakimoto, S. Ueki, H. Kimura, Y. Endoh, S. Hosoya, G. Shirane, R. J. Birgeneau, M. Greven, M. A. Kastner, and Y. J. Kim, Doping dependence of the spatially modulated dynamical spin correlations and the superconducting-transition temperature in $La_{2-x}Sr_xCuO_4$, Phys. Rev. B **57**, 6165 (1998).

[7] S. Wakimoto, R. J. Birgeneau, M. A. Kastner, Y. S. Lee, R. Erwin, P. M. Gehring, S. H. Lee, M. Fujita, K. Yamada, Y. Endoh, K. Hirota, and G. Shirane, Direct observation of a one-dimensional static spin modulation in insulating $La_{1.95}Sr_{0.05}CuO_4$, Phys. Rev. B **61**, 3699 (2000).

[8] S. Wakimoto, G. Shirane, Y. Endoh, K. Hirota, S. Ueki, K. Yamada, R. J. Birgeneau, M. A. Kastner, Y. S. Lee, P. M. Gehring, and S. H. Lee, Observation of incommensurate magnetic correlations at the lower critical concentration for superconductivity in $La_{2-x}Sr_xCuO_4$ ($x = 0.05$), Phys. Rev. B **60**, R769 (1999).

[9] M. Fujita, K. Yamada, H. Hiraka, P. Gehring, S. Lee, S. Wakimoto, and G. Shirane, Static magnetic correlations near the insulating-superconducting phase boundary in $La_{2-x}Sr_xCuO_4$, Phys. Rev. B **65**, 064505 (2002).

[10] E. Demler, W. Hanke, and S.-C. Zhang, SO(5) theory of antiferromagnetism and superconductivity, Rev. Mod. Phys. **76**, 909 (2004).

[11] D. E. Almeida, R. M. Fernandes, and E. Miranda, Induced spin-triplet pairing in the coexistence state of antiferromagnetism and singlet superconductivity: Collective modes and microscopic properties, Phys. Rev. B **96**, 014514 (2017).

[12] A. Himeda and M. Ogata, Coexistence of $d_{x_2-y_2}$ superconductivity and antiferromagnetism in the two-dimensional $t-J$ model and numerical estimation of Gutzwiller factors, Phys. Rev. B **60**, R9935 (1999).

[13] S. Verret, M. Charlebois, D. Sénéchal, and A.-M. S. Tremblay, Subgap structures and pseudogap in cuprate superconductors: Role of density waves, Phys. Rev. B **95**, 054518 (2017).

[14] P. A. Lee, Amperean Pairing and the Pseudogap Phase of Cuprate Superconductors, Phys. Rev. X **4**, 031017 (2014).

[15] M. R. Norman and J. C. Séamus Davis, Quantum oscillations in a biaxial pair density wave state, Proc. Natl. Acad. Sci. USA **115**, 5389 (2018).

[16] M. H. Hamidian, S. D. Edkins, S. H. Joo, A. Kostin, H. Eisaki, S. Uchida, M. J. Lawler, E.-A. Kim, A. P. Mackenzie, K. Fujita, J. Lee, and J. C. Séamus Davis, Detection of a Cooper-pair density wave in $Bi_2Sr_2CaCu_2O_{8+x}$, Nature (London) **532**, 343 (2016).

[17] M. Inui, S. Doniach, P. Hirschfeld, and A. Ruckenstein, Coexistence of antiferromagnetism and superconductivity in a mean-field theory of high-T_c superconductors, Phys. Rev. B **37**, 2320 (1988).

[18] B. Kyung, Mean-field study of the interplay between antiferromagnetism and d-wave superconductivity, Phys. Rev. B **62**, 9083 (2000).

[19] D. Sénéchal, P.-L. Lavertu, M.-A. Marois, and A.-M. S. Tremblay, Competition between Antiferromagnetism and Superconductivity in High-T_c Cuprates, Phys. Rev. Lett. **94**, 156404 (2005).

[20] M. Capone and G. Kotliar, Competition between d-wave superconductivity and antiferromagnetism in the two-dimensional Hubbard model, Phys. Rev. B **74**, 054513 (2006).

[21] S. S. Kancharla, B. Kyung, D. Sénéchal, M. Civelli, M. Capone, G. Kotliar, and A.-M. S. Tremblay, Anomalous superconductivity and its competition with antiferromagnetism in doped Mott insulators, Phys. Rev. B **77**, 184516 (2008).

[22] J. Reiss, D. Rohe, and W. Metzner, Renormalized mean-field analysis of antiferromagnetism and d-wave superconductivity in the two-dimensional Hubbard model, Phys. Rev. B **75**, 075110 (2007).

[23] H. Yamase, A. Eberlein, and W. Metzner, Coexistence of Incommensurate Magnetism and Superconductivity in the Two-Dimensional Hubbard Model, Phys. Rev. Lett. **116**, 096402 (2016).

[24] E. Koch, G. Sangiovanni, and O. Gunnarsson, Sum rules and bath parametrization for quantum cluster theories, Phys. Rev. B **78**, 115102 (2008).

[25] A. Liebsch and N.-H. Tong, Finite-temperature exact diagonalization cluster dynamical mean-field study of the two-dimensional Hubbard model: Pseudogap, non-Fermi-liquid behavior, and particle-hole asymmetry, Phys. Rev. B **80**, 165126 (2009).

[26] A. Liebsch and H. Ishida, Temperature and bath size in exact diagonalization dynamical mean field theory, J. Phys.: Condens. Matter **24**, 053201 (2012).

[27] E. Gull, A. J. Millis, A. I. Lichtenstein, A. N. Rubtsov, M. Troyer, and P. Werner, Continuous-time Monte Carlo methods for quantum impurity models, Rev. Mod. Phys. **83**, 349 (2011).

[28] M. Jarrell, Th. Maier, M. H. Hettler, and A. N. Tahvildarzadeh, Phase diagram of the Hubbard model: Beyond the dynamical mean field, Europhys. Lett. **56**, 563 (2001).

[29] Th. A. Maier, M. Jarrell, A. Macridin, and C. Slezak, Kinetic Energy Driven Pairing in Cuprate Superconductors, Phys. Rev. Lett. **92**, 027005 (2004).

[30] T. A. Maier, M. Jarrell, T. C. Schulthess, P. R. C. Kent, and J. B. White, Systematic Study of d-Wave Superconductivity in the 2D Repulsive Hubbard Model, Phys. Rev. Lett. **95**, 237001 (2005).

[31] G. Sordi, P. Sémon, K. Haule, and A.-M. S. Tremblay, Strong Coupling Superconductivity, Pseudogap, and Mott Transition, Phys. Rev. Lett. **108**, 216401 (2012).

[32] N. Lin, E. Gull, and A. J. Millis, Two-Particle Response in Cluster Dynamical Mean-Field Theory: Formalism and Application to the Raman Response of High-Temperature Superconductors, Phys. Rev. Lett. **109**, 106401 (2012).

[33] E. Gull, O. Parcollet, and A. J. Millis, Superconductivity and the Pseudogap in the Two-Dimensional Hubbard Model, Phys. Rev. Lett. **110**, 216405 (2013).

[34] E. Gull and A. J. Millis, Energetics of superconductivity in the two-dimensional Hubbard model, Phys. Rev. B **86**, 241106 (2012).

[35] G. Sordi, P. Sémon, K. Haule, and A.-M. S. Tremblay, c-axis resistivity, pseudogap, superconductivity, and Widom line in doped Mott insulators, Phys. Rev. B **87**, 041101 (2013).

[36] E. Gull and A. J. Millis, Superconducting and pseudogap effects on the interplane conductivity and Raman scattering cross section in the two-dimensional Hubbard model, Phys. Rev. B **88**, 075127 (2013).

[37] P. Staar, T. A. Maier, M. S. Summers, G. Fourestey, R. Solca, and T. C. Schulthess, Taking a quantum leap in time to solution for simulations of high-Tc superconductors, in SC'13: Proceedings of the International Conference for High Performance Computing, Networking, Storage and Analysis (ACM Press, Denver, 2013), pp. 1–11.

[38] P. Sémon, G. Sordi, and A.-M. S. Tremblay, Ergodicity of the hybridization-expansion Monte Carlo algorithm for broken-symmetry states, Phys. Rev. B **89**, 165113 (2014).

[39] E. Gull and A. J. Millis, Pairing glue in the two-dimensional Hubbard model, Phys. Rev. B **90**, 041110 (2014).

[40] E. Gull and A. J. Millis, Quasiparticle properties of the superconducting state of the two-dimensional Hubbard model, Phys. Rev. B **91**, 085116 (2015).

[41] L. Fratino, P. Sémon, G. Sordi, and A.-M. S. Tremblay, An organizing principle for two-dimensional strongly correlated superconductivity, Sci. Rep. **6**, 22715 (2016).

[42] A. Reymbaut, M. Charlebois, M. F. Asiani, L. Fratino, P. Sémon, G. Sordi, and A.-M. S. Tremblay, Antagonistic effects of nearest-neighbor repulsion on the superconducting pairing dynamics in the doped Mott insulator regime, Phys. Rev. B **94**, 155146 (2016).

[43] L. Fratino, P. Sémon, M. Charlebois, G. Sordi, and A.-M. S. Tremblay, Signatures of the Mott transition in the antiferromagnetic state of the two-dimensional Hubbard model, Phys. Rev. B **95**, 235109 (2017).

[44] L. Fratino, M. Charlebois, P. Sémon, G. Sordi, and A.-M. S. Tremblay, Effects of interaction strength, doping, and frustration on the antiferromagnetic phase of the two-dimensional Hubbard model, Phys. Rev. B **96**, 241109 (2017).

[45] S. Sakai, G. Sangiovanni, M. Civelli, Y. Motome, K. Held, and M. Imada, Cluster-size dependence in cellular dynamical mean-field theory, Phys. Rev. B **85**, 035102 (2012).

[46] G. Biroli and G. Kotliar, Cluster methods for strongly correlated electron systems, Phys. Rev. B **65**, 155112 (2002).

[47] K. Aryanpour, Th. A. Maier, and M. Jarrell, Comment on "Cluster methods for strongly correlated electron systems," Phys. Rev. B **71**, 037101 (2005).

[48] G. Biroli and G. Kotliar, Reply to "Comment on 'Cluster methods for strongly correlated electron systems,' " Phys. Rev. B **71**, 037102 (2005).

[49] J. Zaanen, G. A. Sawatzky, and J. W. Allen, Band Gaps and Electronic Structure of Transition-Metal Compounds, Phys. Rev. Lett. **55**, 418 (1985).

[50] O. K. Andersen, A. I. Liechtenstein, O. Jepsen, and F. Paulsen, LDA energy bands, low-energy Hamiltonians, t', t'', $t \perp (k)$, and $J \perp$, J. Phys. Chem. Solids **56**, 1573 (1995).

[51] B. Kyung, V. Hankevych, A.-M. Daré, and A.-M. S. Tremblay, Pseudogap and Spin Fluctuations in the Normal State of the Electron-Doped Cuprates, Phys. Rev. Lett. **93**, 147004 (2004).

[52] R. S. Markiewicz, I. G. Buda, P. Mistark, C. Lane, and A. Bansil, Entropic origin of pseudogap physics and a mott-slater transition in cuprates, Sci. Rep. **7**, 44008 (2017).

[53] M. Caffarel and W. Krauth, Exact Diagonalization Approach to Correlated Fermions in Infinite Dimensions: Mott Transition and Superconductivity, Phys. Rev. Lett. **72**, 1545 (1994).

[54] D. Sénéchal, Bath optimization in the cellular dynamical mean-field theory, Phys. Rev. B **81**, 235125 (2010).

[55] D. Sénéchal, Cluster Dynamical Mean Field Theory, in *Strongly Correlated Systems*, Springer Series in Solid-State Sciences Vol. 171, edited by A. Avella and F. Mancini (Springer, Berlin, 2012), pp. 341–371.

[56] See Supplemental Material at http://link.aps.org/supplemental/10.1103/PhysRevB.99.184510 for phase diagrams made with other combinations of lattice and cluster averages and for comments on the differences between them.

[57] M. Guillot, Compétition entre l'antiferromagnétisme et la supraconductivité dans le modèle et Hubbard appliqué aux cuprates, M.Sc. thesis, Université de Sherbrooke, 2007.

[58] M. Aichhorn, E. Arrigoni, M. Potthoff, and W. Hanke, Antiferromagnetic to superconducting phase transition in the hole- and electron-doped Hubbard model at zero temperature, Phys. Rev. B **74**, 024508 (2006).

[59] S. Sachdev, Quantum criticality and the phase diagram of the cuprates, Physica C (Amsterdam, Neth.) **470**, S4 (2010).

[60] R. Comin and A. Damascelli, Resonant X-Ray Scattering Studies of Charge Order in Cuprates, Annu. Rev. Condens. Matter Phys. **7**, 369 (2016).

[61] D. Haug, V. Hinkov, Y. Sidis, P. Bourges, N. B. Christensen, A. Ivanov, T. Keller, C. T. Lin, and B. Keimer, Neutron scattering study of the magnetic phase diagram of underdoped $YBa_2Cu_3O_{6+x}$, New J. Phys. **12**, 105006 (2010).

[62] A. Eberlein, W. Metzner, S. Sachdev, and H. Yamase, Fermi Surface Reconstruction and Drop in the Hall Number due to Spiral Antiferromagnetism in High-T_c Cuprates, Phys. Rev. Lett. **117**, 187001 (2016).

[63] Y. M. Vilk and A.-M. S. Tremblay, Non-perturbative many-body approach to the hubbard model and single-particle pseudogap, J. Phys. I **7**, 1309 (1997).

[64] H. J. Schulz, Incommensurate Antiferromagnetism in the Two-Dimensional Hubbard Model, Phys. Rev. Lett. **64**, 1445 (1990).

[65] J. P. L. Faye and D. Sénéchal, Interplay between d-wave superconductivity and a bond-density wave in the one-band Hubbard model, Phys. Rev. B **95**, 115127 (2017).

[66] M. Charlebois, S. Verret, A. Foley, O. Simard, D. Sénéchal, and A.-M. S. Tremblay, Hall effect in cuprates with an incommensurate collinear spin-density wave, Phys. Rev. B **96**, 205132 (2017).

[67] S. Verret, O. Simard, M. Charlebois, D. Sénéchal, and A.-M. S. Tremblay, Phenomenological theories of the low-temperature pseudogap: Hall number, specific heat, and Seebeck coefficient, Phys. Rev. B **96**, 125139 (2017).